A&A 426, 1035–1045 (2004)
DOI: 10.1051/0004-6361:20040494

Astronomy & Astrophysics

X-ray spectroscopy of the W UMa-type binary 44 Bootis

P. Gondoin

European Space Agency, ESTEC – Postbus 299, 2200 AG Noordwijk, The Netherlands
e-mail: pgondoin@rssd.esa.int

Received 22 March 2004 / Accepted 1 July 2004

Abstract. 44 Boo B, a W UMa-type binary system, was observed in June 2001 during one entire revolution period with the *XMM–Newton* observatory. The count rate in the 0.3 to 2 keV band is constant in average with 5 to 20% count rate increases reminiscent of flares. Spectral fitting of the EPIC spectra indicates a corona configuration with little contribution from quiet regions, similar to the Sun. On the contrary, the (2–9) $\times$ 10^6 K temperature range of the "cool" plasma suggests that the active corona around the two companions is densely filled with low-lying loops similar to those found in solar-type active regions. The 44 Boo O VII He-like triplet constrains the electron density to an upper limit $n_e < 8.6 \times 10^{10}$ cm^{-3}. We argue that this low-lying loop system may be overlaid by larger loops. Magnetic reconnection phenomena in this large loops system may explain the characteristic flare decay time in the light curve that implies loop lengths of about 16×10^9 cm. An extended corona around 44 Boo would explain the absence of eclipses in its X-ray light curve. The average element abundance in 44 Boo corona is found to be lower than the solar photospheric value. The spectral analysis indicates enhanced abundances of oxygen and neon relative to iron which suggest an inverse FIP effect. Compared with other active binary systems such as RSCVn or BY Dra, 44 Boo has relatively less material at temperatures higher than 10^7 K and the temperature of its hottest plasma component appears to be lower.

Key words. stars: individual: 44 Bootis – stars: activity – stars: coronae – stars: late-type – X-rays: stars – stars: binaries: general

1. Introduction

44 Bootis B (HD 133640 = BD+48°2259; $V = 4.76$) is the nearest contact binary and one of the nearest close binary system ($\pi = 0.078 \pm 0.001''$; ESA 1997) with an extremely fast rotation and revolution period of only 0.268 days. It is a well-known representative of the WUMa stellar class which consists of eclipsing binaries with late F–K spectral type components in contact via a common convective envelope. Strong tidal forces cause them to rotate synchronously. 44 Boo B (HD 133640), one of the most frequently photometrically observed variable star, is a partial eclipsing contact binary with components of spectral type G2V+G (Hill et al. 1989). Lu et al. (2001) argue that the color index for component B points at a later spectral type around K2 V. The two minima of the optical light curve are unequal in depth (Schilt 1926). The primary eclipse (phase 0.0) corresponds to the eclipse of the secondary by the primary, characteristic of a W-type system (Rucinski 1985). 44 Boo B is the fainter member of the visual binary system ADS 9494 with a period of 225 years. It is generally assumed that the contact binary produces all activity related phenomena (see Vilhu et al. 1989). A comparison of the relative line fluxes for selected strongest chromospheric, transition region, and low corona emission lines in 44 Boo and a single rapidly rotating reference star showed that *Extreme Ultraviolet Explorer* data obtained in 1995 were consistent with period-independent saturated levels of activity for features forming at $T \leq 10^5$ K (Rucinski 1998). A 130 h observation of 44 Boo with the spectrometer and the Deep Survey instrument on-board of *Extreme Ultraviolet Explorer* showed a sinusoidal variation of the EUV flux with a period close to the orbital period (Brickhouse & Dupree 1998). These variations were interpreted as an indication of the presence of an active region on the primary component of the binary.

WUMa type stars are strong X-ray emitters but with luminosities lower, in general, than those of the detached, subgiant RS CVn type binaries, possibly due to saturation effects (Vilhu & Heise 1986; Stepien et al. 2001; Gondoin 2004). Since the components in W UMa systems have the shortest periods possible for two non-degenerate main-sequence stars, these objects are of great interest in the study of the relation between stellar rotation rate and X-ray activity. Observations of 44 Boo with the Imaging Proportional Counter (IPC) and with the Solid State Spectrometer on board *Einstein* suggest the existence of a hot corona (Cruddace & Dupree 1984). The X-ray light curves (Cruddace & Dupree 1984; Vilhu & Heise 1986) do not show evidence for phase modulation. On the contrary, X-ray light curve measurements by *Einstein* and *EXOSAT* show erratic variability, including occasional rapid flux changes. Cruddace & Dupree (1984) conclude that 44 Boo B has an extended corona, consistent with the absence of an X-ray eclipse. Schmitt et al. (1990) discussed the

Table 1. 44 Bootis observation log during revolution 274.

Rev.	Experiment	Filter	Mode	Start Exp.(UT)	Exp. Duration
274	p−n	Thick	Full frame	2001-06-08@11:27:12	30 716 s
	RGS1		Spec + Q	2001-06-08@10:42:54	33 141 s
	RGS2		Spec + Q	2001-06-08@10:42:54	33 223 s

low-resolution observed X-ray spectra of 44 Boo and showed them to be consistent with a two temperatures thermal emission model. McGale et al. (1996) also found a model, with temperatures of around 1.8×10^6 K and 10^7 K, consistent with the *ROSAT* PSPC data. They noted that the light curve of 44 Boo appears constant during the short 1678 ks observation. *Chandra* High-Energy Transmission Grating observations of 44 Boo on April 2000 show an X-ray emission spectrum with strong O VIII, Ne X, Fe XVII and Mg XII emission lines which centroids position vary with orbital phase (Brickhouse et al. 2001). The phase dependence of line profiles and light curves together imply that at least half of the X-ray emission was localized at high latitude, possibly on the primary star.

We provide analysis results of X-ray spectra of 44 Boo registered during an observation performed in June 2001 with the *XMM−Newton* observatory. The paper is organized as follows. Section 2 describes the X-ray observations of 44 Boo and the data reduction procedures. Section 3 presents the integrated flux measurements and their temporal behavior during the observations. Sections 4 and 5 describe the spectral analysis of the EPIC and RGS data sets, respectively. An interpretation of the analysis results is given in Sect. 6 and the study results are summarized in Sect. 7.

2. Observations and data reduction

44 Bootis was observed by the *XMM−Newton* space observatory (Jansen et al. 2001), in revolution 274 on 2001 June 8 (see Table 1). The satellite observatory uses three grazing incidence telescopes which provide an effective area higher than 4000 cm^2 at 2 keV and 1600 cm^2 at 8 keV (Gondoin et al. 2000). One CCD EPIC pn camera (Strüder et al. 2001) and two EPIC MOS cameras (Turner et al. 2001) at the prime focus of the telescopes provide imaging in a 30 arcmin field of view and broadband spectroscopy with a resolving power of between 10 and 60 in the energy band 0.3 to 10 keV. Two identical RGS reflection grating spectrometers behind two of the three X-ray telescopes allow higher resolution ($E/\Delta E$ = 100 to 500) measurements in the soft X-ray range (6 to 38 Å or 0.3 to 2.1 keV) with a maximum effective area of about 140 cm^2 at 15 Å (den Herder et al. 2001).

44 Bootis observations were conducted with the EPIC pn camera operating in full frame mode (Ehle et al. 2001). RGS spectra were recorded simultaneously. A "thick" aluminum filter was used in front of the EPIC camera to reject visible light from the star itself. Processing of the raw event dataset was performed using the "emchain", "epchain" and "rgsproc" pipeline tasks of the *XMM−Newton* Science Analysis System (SAS version 5.3.0). The large count rate of the target produced pile-up effects in the core of the telescope point spread function registered by the EPIC pn camera. In order to reject these ambiguous events, the source spectra were built from photons detected within an annulus of radius included between 11″ and 62″ from the target boresight. The background was estimated on the same CCD chip within a circular window of 54″ radius which were offset from the source centroid position. Background rate in the EPIC pn camera was found to be extremely low during the first 25 ks of the observation. Due to a large increase of the background rate, the last 6 ks of the EPIC pn event list was rejected. The Pulse-Invariant (PI) spectra were rebinned such that each resulting pn channel had at least 50 counts per bin. χ^2 minimization was used for spectral fitting. All fits were performed using the XSPEC package (Arnaud & Dorman 2001). The EPIC and RGS response matrices were generated by the SAS task "rmfgen" and "rgsrmfgen" respectively. The EPIC p−n and RGS spectra were analyzed separately due to their different spectral resolution and spectral band coverage.

3. Integrated flux and temporal behaviour

Due to rising background level towards the end of the observation, only the first 25 ks of the EPIC pn data could be reliably analysed out of the 31 ks observation period. This duration is just above one orbital period of the 44 Boo B contact binary system. Figure 1 shows the X-ray light curve of 44 Bootis. The orbital phase during the *XMM−Newton* observation was derived from the orbital elements provided by Lu et al. (2001). The count rate in the 0.3 to 2 keV band is about 10 s^{-1} in average with 5 to 20% count rate increases around phases 1.3, 1.65 and 1.9. These rapid count rate variations are reminiscent of flares found by Brickhouse et al. (2001) in recent *Chandra* observations. The hardness ratio of the hard to soft energy light curves (see Fig. 1) supports this hypothesis and indicate that these bumps are not gray intensity changes that would be expected from the rotational modulation of uniform structures.

The spectral analysis of the observation was conducted separately for two analysis periods. The first analysis period corresponds to three time intervalls of respectively 2 ks, 2.2 ks and 1.2 ks centred around phase 1.3, 1.65 and 1.9 possibly associated with flares. The second analysis period corresponds to the relatively steady flux level observed during the remaining part of the observation. Spectral fitting of EPIC data (see Sect. 4) yields flux measurements in the 0.3−2 keV and 2−10 keV bands. These measurements were converted into X-ray luminosities $L_{0.3-2\ \mathrm{keV}}$ and $L_{>2\ \mathrm{keV}}$ using *Hipparcos* parallax data (ESA 1997). Results are given in Table 2 including hardness ratios *hr* of the X-ray emission defined as $hr = (L_{>2\ \mathrm{keV}} - L_{0.3-2\ \mathrm{keV}})/(L_{>2\ \mathrm{keV}} + L_{0.3-2\ \mathrm{keV}})$. The X-ray spectrum of 44 B Boo is soft during both revolutions. The X-ray

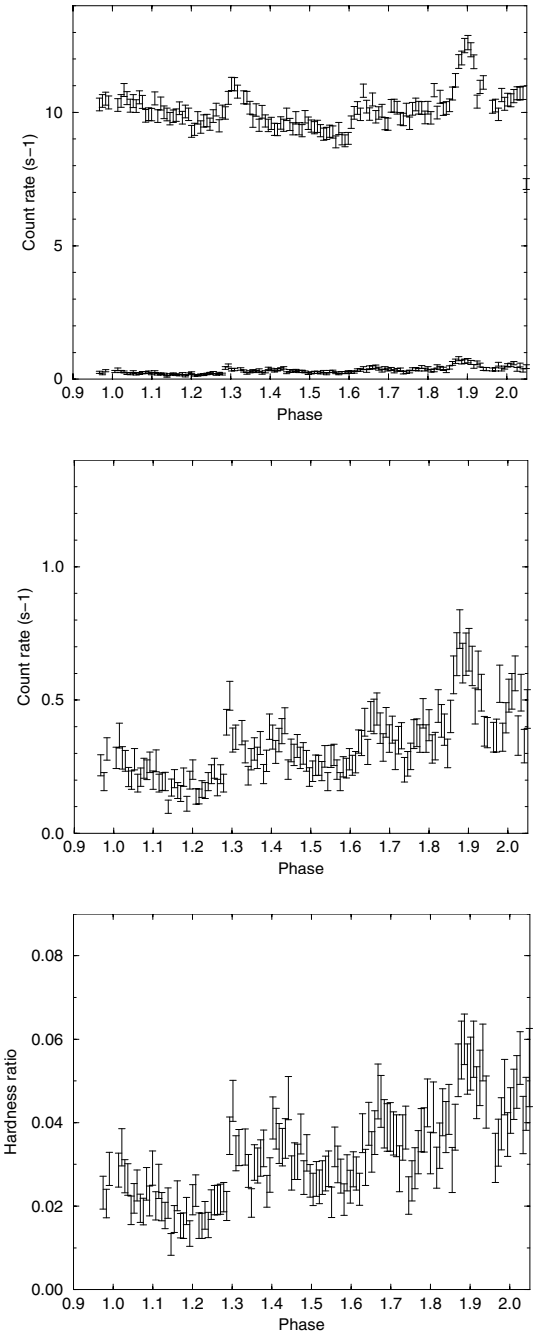

Fig. 1. Light curves and hardness ratio of 44 Boo. In the top panel, the upper curve is the count rate in the 0.3 to 2 keV band and the lower curve is the count rate in the 2 to 10 keV band. This light curve is expanded in the middle panel. The lower panel shows the hardness ratio between the high and low energy bands. The events are binned in 180 s time intervals and the background contribution has been subtracted.

luminosity is more than 10 times higher in the 0.3–2 keV band than in the 2–5 keV. Table 2 indicates that the luminosity increases during the flare periods by about 10% in the 0.3–2 keV band and by 54% in the 2–5 keV band. There is an important contribution of plasma hotter than $kT > 1$ keV during both periods. However, during the steady count rate period, the emission measure distribution of the hottest plasma component is centred at a lower temperature than during the flare period (see Sect. 4).

Table 2. X-ray luminosities of 44 Boo in the 0.3−2 keV and 2−5 keV energy bands averaged over the different observations periods and corrected for interstellar absorption. The percentage contribution in flux of hot plasmas ($kT \geq 1$ keV) is indicated between bracketts.

Obs.	$L_{0.3-2\mathrm{keV}}$ (10^{28} erg s^{-1})	$L_{>2\mathrm{keV}}$ (10^{28} erg s^{-1})	hr
Rev. 274	24.3	2.0	–0.85
(flares)	(30%)	(77%)	
Rev. 274	22.4	1.3	–0.89
(steady rate)	(36%)	(78%)	

Table 3. Best fit parameters to EPIC data using a 3 components MEKAL model (Mewe et al. 1985). The spectral fitting was conducted in the 0.3–5 keV band with the same abundance relative to the Sun for all components.

	Flares period	Quiescent period
N_{H} (cm^{-2})	10^{18} (frozen)	10^{18} (frozen)
Z	0.28 ± 0.02	0.22 ± 0.01
kT_1 (keV)	0.31 ± 0.02	0.25 ± 0.01
EM_1 (10^{52} cm^{-3})	0.85 ± 0.13	0.59 ± 0.07
kT_2 (keV)	0.71 ± 0.03	0.61 ± 0.01
EM_2 (10^{52} cm^{-3})	1.07 ± 0.11	1.24 ± 0.07
kT_3 (keV)	1.32 ± 0.06	1.05 ± 0.02
EM_3 (10^{52} cm^{-3})	0.93 ± 0.09	1.02 ± 0.07
χ^2	0.87 (204/234 d.o.f.)	1.31 (435/332 d.o.f.)

4. Spectral analysis of EPIC data

The two EPIC datasets (see Fig. 2) were fitted separately with the MEKAL optically thin plasma emission model (Mewe et al. 1985). The spectral fitting was performed in the 0.3–5 keV spectral bands for both analysis periods. The interstellar hydrogen column density was fixed to the value $N_{\mathrm{H}} = 10^{18}$ cm^{-2} derived from *IUE* measurements of the Lyα profile (Vilhu et al. 1989) and also adopted by Brickhouse & Dupree (1998). No single temperature plasma model that assumes either solar photospheric (Anders & Grevesse 1989) or non-solar abundances can fit the data, as unacceptably large values of χ^2 are obtained. A MEKAL plasma model with two components at different temperatures proves not acceptable. Hence, the EPIC spectra were fitted using a MEKAL model with three components at different temperatures but having the same metallicity. The addition of a fourth component to the model does not improve the quality of the spectral fit.

The temperatures of the coolest plasma components varies in the range $T \approx (2\text{–}4) \times 10^6$ K and $(7\text{–}9) \times 10^6$ K and are slightly higher during the flare periods. The temperature of the hottest plasma component varies in the range $(1.2\text{–}1.6) \times 10^7$ K between the two analysis periods with a higher temperature during the flare periods. The average element abundance in the 44 Boo corona is found to be lower than the solar photospheric value (see Table 3). No significant abundance variation

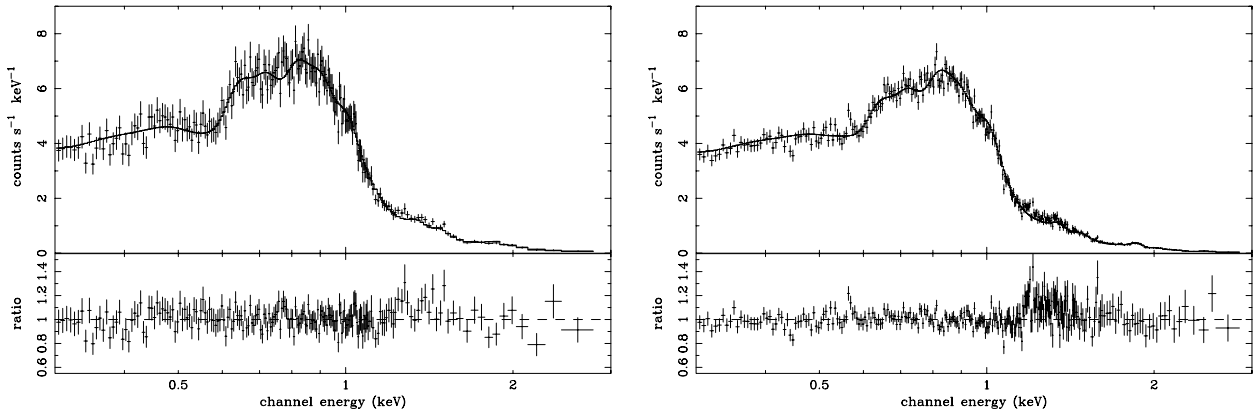

Fig. 2. Best fit MEKAL model (see Table 3) to EPIC spectra during the flare periods (*left*) and during the intermediate steady flux period (*right*). The EPIC data (crosses) and spectral fit (solid line) are shown in the upper panel. Their ratio is shown in the lower panel of each graph.

is detected between the two analysis periods. The three components model suggests that more than 60% of the emission measure is related to plasmas with temperatures in the range (2–9) $\times$ 10^6 K. These are the main sources of X-ray emission in the soft energy band below 2 keV. Hot ($T > 10^7$ K) plasmas in 44 Boo have a lower emission measure but are the main source of emission in the hard X-ray band above 2 keV. They contribute to more than 75% of the X-ray luminosity above 2 keV. Among all of the different changes, eruption and instabilities seen on the Sun, the ones labeled "flares" all have in common material heated to temperatures of 10^7 K or higher (Golub & Pasachoff 1997; Reale et al. 2001). In active stellar coronae, it has been proposed that the peak in emission measure around 10^7 K is due to flaring activity (Drake et al. 2000; Sanz-Forcada et al. 2002). Bright flares are expected to induce count rate fluctuations in the X-ray light curves of active stars. Thus, the existence of significant amounts of $>10^7$ K material in 44 Boo corona and the count rate fluctuations in its light curve are indicative of a high flaring activity. The occurrence of flares on 44 Bootis is corroborated by the temperature increase of the different plasma components during the high count rate periods.

As spatially unresolved observations gain in spectral resolution and signal to noise ratio, the amount of details in the spectra of stellar coronae which must be reproduced increases reflecting the true complexity of the sources plasma. Multi-temperature models are now necessary to explain high-resolution spectra of bright stellar coronae (Dupree et al. 1993; Griffiths & Jordan 1998; Bowyer et al. 2000). Recent analysis of *XMM−Newton* and *Chandra* X-ray spectra find that a continuous emission measure distribution fits the data better and is more realistic physically (Audard et al. 2001a,b; Güdel et al. 2001; Mewe et al. 2001). We fitted the EPIC spectra of 44 Boo with a plasma emission model built from the MEKAL code in which the emission measure distribution follows a power-law in temperature of the forme $EM_{\max} \times (T/T_{\max})^{\alpha}$ (see Fig. 3). The model was used with four free parameters, i.e. the normalization constant $EM_{\max}$, the maximum temperature $T_{\max}$, the abundance and the slope α of the emission measure distribution. This functional form turns out to describe the differential emission measure distribution of isolated solar coronal loops very well (see Antiochos & Noci 1986). The power law slope α is related to the power law coefficient β of the radiative cooling function approximated by $P(T) \approx T^{\beta}$ through $\alpha = 3/4 + \beta/2$. For ensembles of coronal hot loops, Antiochos & Noci (1986) found that the differential emission measure distribution is dominated by loops with the highest temperature and density. Therefore the equation $EM_{\max} \times (T/T_{\max})^{\alpha}$ also applies for an ensemble of loops at temperature in excess of 10^6 K. Table 4 lists the best fit parameters derived when applying the power law model to the EPIC spectra obtained during the flare periods (left) and during the intermediate steady flux periods. The normalisation and power law slope are comparable for the two analysis periods. The maximum temperature $T_{\max}$ of the emission measure distribution is higher during period of high count rate than during the quiescent period. This maximum temperature is equal to the temperature of the hottest plasma component in the three component MEKAL model (see Table 3). The best fit power-law index of the emission measure distributions is close to 1 both during the flares and the quiescent periods. This value contrasts with the rather large values of α which are found for low-gravity objects, i.e. giants and RS CVn systems (Schmitt et al. 1990). Large values of α are a reflection of the fact that most of the emission is concentrated at the maximum temperature. 44 Boo, on the contrary, has an emission measure distribution with a slope near unity similar to those measured for main-sequence stars (Schmitt et al. 1990), consistent with solar-type loops (i.e. loops with constant cross-section) being responsible for the X-ray emission. The emission measure of hot plasmas is spread over temperature, in agreement with the result obtained using a three components MEKAL model which give similar values of the emission measure at different temperatures (see Table 3). The abundance derived from the three component MEKAL model and from the power-law emission measure distribution model are similar and the fitting quality is comparable.

5. Spectral analysis of RGS data

5.1. Line identification

Because of the lower effective area and larger spectral resolution of the RGS experiment compared with the

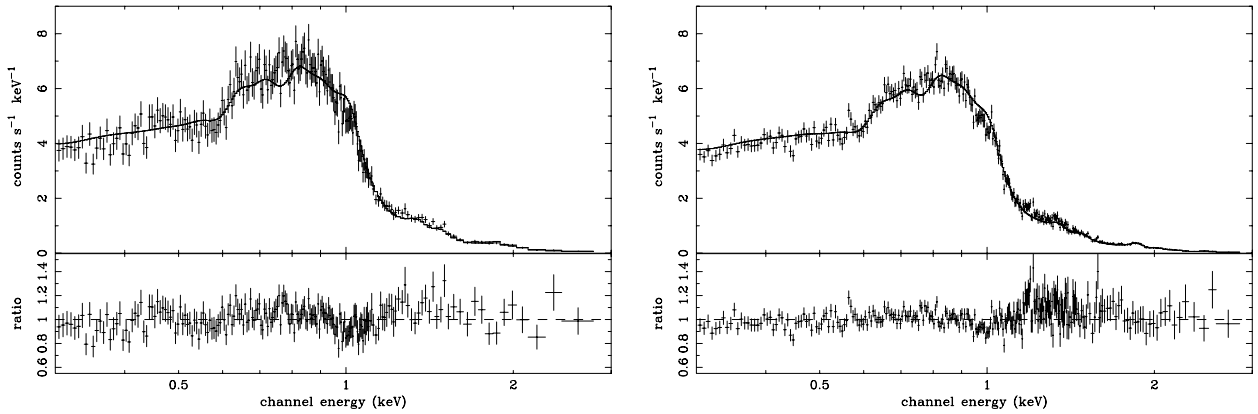

Fig. 3. Best fit model (using a power-law emission measure distribution; see Table 4) to EPIC spectra during the flare periods (*left*) and during the intermediate steady flux period (*right*). The EPIC data (crosses) and spectral fit (solid line) are shown in the upper panel. Their ratio is shown in the lower panel of each graph.

Table 4. Best fit parameters to EPIC data using a plasma emission model built from the MEKAL code in which the emission measure distribution follows a power-law in temperature of the forme $EM_{\max} \times (T/T_{\max})^{\alpha}$.

	Flares period	Quiescent period
$N_{\rm H}$ (cm^{-2})	10^{18} (frozen)	10^{18} (frozen)
Z	0.31 ± 0.02	0.24 ± 0.08
$kT_{\max}$ (keV)	1.31 ± 0.05	1.08 ± 0.02
α	0.84 ± 0.07	1.03 ± 0.05
$EM_{\max}$ (10^{52} cm^{-3})	5.5 ± 0.5	6.6 ± 0.3
χ^2	1.09 (259/237 d.o.f.)	1.45 (487/335 d.o.f.)

EPIC camera, we did not divide the RGS exposures in periods corresponding to low and high count rates. This approach provides higher signal to noise ratio spectra at the expense of time resolution. EPIC analysis results will be kept in mind which indicate that the X-ray emission was variable during the observation. Figure 4 shows the RGS spectra of 44 Boo averaged over the 33 ks RGS exposure. The spectrum is the sum of the two spectra simultaneously obtained with the RGS1 and RGS2 reflection grating spectrometers on board *XMM–Newton*. Line fluxes and positions were measured using the XSPEC package by fitting simultaneously the RGS1 and RGS2 spectra with a sum of narrow Gaussian emission lines convolved with the response matrices of the RGS instruments. The continuum emission was described using Bremstrahlung models at the temperatures of the plasma components inferred from the analysis of EPIC data. The emission measure derived from the analysis of the EPIC data (see Table 3) was used to freeze the continuum normalization. The best fit model using a three temperature Bremstrahlung continuum and Gaussian lines is compared with the data in Fig. 5 to convey the quality of the fitting procedure. For line identification, we required only that the wavelength coincidence be comparable to the spectral resolution of the RGS spectrometers, namely 0.04 Å over the 5 to 35 Å wavelength range. In the X-ray domain, several candidate lines may exist within this acceptable wavelength coincidence range. Series of lines of highly ionized Fe and several lines of the Ly series are visible in RGS spectra, most notably from O and Ne. Table 5 lists the measurements of lines that are statistically significant and gives the line fluxes corrected for interstellar absorption ($N_{\rm H} = 10^{18}$ cm^{-2}) on the line of sight to 44 Boo. Their temperatures of maximum formation range between 1.6×10^6 K and 1.6×10^7 K indicating that the corresponding ions are associated with the plasma component inferred from EPIC data. Lines such as the O VIII and Ne X lines have emissivity functions quite spread in temperature. The flux of the O VIII λ18.97 line (see Table 5) is similar to the value measured by Brickhouse et al. (2001) in *Chandra* spectra obtained in April 2000. In contrast, the fluxes of the Ne X λ12.13, Fe XVII λ15.01 and Mg XII λ8.42 lines are higher in the RGS spectra suggesting that the emission measure of hot plasma ($T > 4$ MK) was in average higher during *XMM–Newton* observations. The flux measurement of some lines such as Ne X λ12.13 is affected by blends.

5.2. The helium-like O VII triplet

Electron densities can be measured using density sensitive spectral lines originating from metastable levels, such as the forbidden (f) 2^3S-1^1S line in helium like ions. This line and the associated resonance (r) 2^1P-1^1S and intercombination (i) 2^3P-1^1S lines make up the so-called helium like triplet lines (Gabriel & Jordan 1969; Pradhan 1982; Mewe et al. 1985). The intensity ratio $G = (i + f)/r$ varies with electron temperature and the ratio $R = f/i$ varies with electron density due to the collisional coupling between the metastable 2^3S upper level of the forbidden line and the 2^3P upper level of the intercombination line. The RGS wavelength band contains the He-like triplets from O VII, Ne IX, Mg XI and Si XIII. However, the Si and Mg triplets are not sufficiently resolved and the Ne IX triplet is too heavily blended with iron lines for unambiguous density analysis. Only the O VII lines are clean, resolved and potentially suited to diagnose plasmas in the density range $n_{\rm e} \approx 10^8$–10^{11} cm^{-3} and temperature range $T \approx 1$–9 MK. The intensity ratio R of the OVII forbiden (λ = 22.12 Å) and intercombination (λ = 21.80 Å) lines calculated using the CHIANTI database (Dere et al. 2001) is plotted in

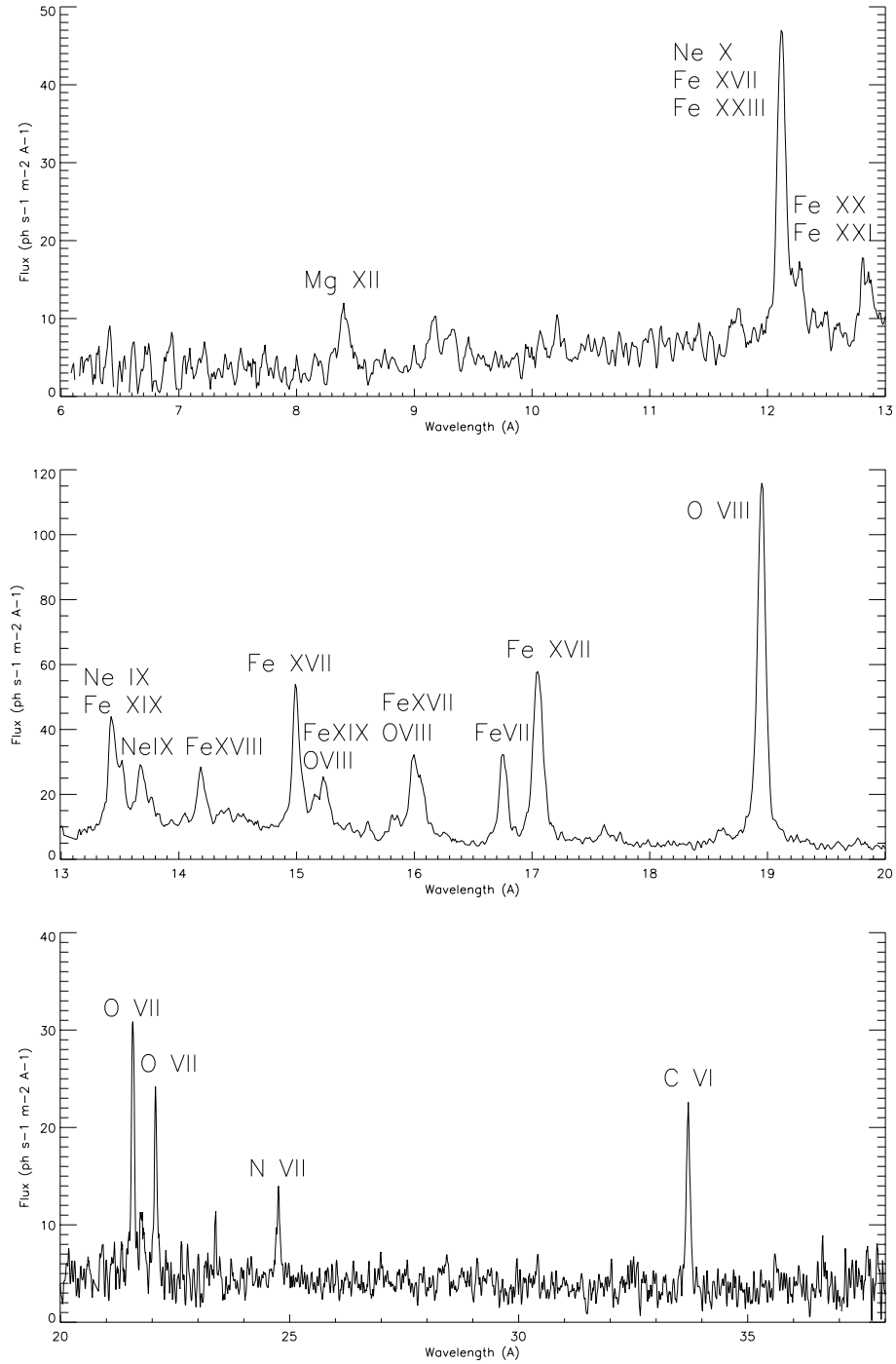

Fig. 4. RGS spectrum of 44 Boo in the 6–38 Å band.

Fig. 6 as a function of electron density. Figure 6 also shows the ratio G of the summed intensity of O VII intercombination and forbiden lines over the intensity of the recombination line ($\lambda = 21.60$ Å) as a function of temperature. The ratio G is independant of electron densities. This ratio for the 44 Boo O VII He-like triplet is in the range 0.48–1.32 (see Table 5) which implies a temperature $T_e \approx (0.6\text{–}4.6) \times 10^6$ K. For this temperature range, the ratio R of the 44 Boo O VII He-like triplet (R = 1.3–7.6; see Table 5) only constrains the electron density to an upper limit $n_e < 8.6 \times 10^{10}$ cm^{-3}. Within these large uncertainties, the best estimate of G and R gives $T_e \approx 2 \times 10^6$ K and $n_e \approx 1.4 \times 10^{10}$ cm^{-3}, i.e. $P_e \approx 7.7$ dyn cm^{-2}. If the X-ray emission of 44 Boo originates from magnetically confined plasma loops, a typical loop length $L \approx 4 \times 10^8$ cm can be deduced from P_e and T_e using the RTV scaling law $T_{max} = 1400 \times (pL)^{1/3}$ (Rosner et al. 1978). The X-ray emission would originate from low-lying magnetic loops similar in size to those found in the solar corona, suggesting that 44 Boo corona has an apparence similar to the Sun's.

Ness et al. (2001) plotted a G vs. R diagram using solar observations of the OVII triplet in the quiescent corona (Freeman & Jones 1970; McKenzie et al. 1978), in active

Table 5. Positions, transition, temperatures of maximum line formation and fluxes of the strongest lines in RGS spectra.

λ_{meas} (Å)	λ_{pred} (Å)	Ion	Transition	log (T_{max}) log (K)	$F_{meas.}$ (10^{-2} m^{-2} s^{-1})
8.42	8.42	Mg XII	$2p^2P_{1/2,3/2}-1s^2S_{1/2}$	7.0	83 ± 25
9.17	9.17	Mg XI	$1s2p^1P_1-1s^2\ ^1S_0$	6.8	92 ± 22
10.24	10.24	Ne X	$3p^2P_{1/2,3/2}-1s^2S_{1/2}$	6.8	73 ± 19
11.74	11.74	Fe XXIII	$1s^22s3d^1D_2-1s^22s2p^1P_1$	7.2	102 ± 27
	11.77	Fe XXII	$1s^22s^23d^1D_{3/2}-1s^22s^22p^2P_{1/2}$	7.1	
12.13	12.13	Ne X	$2p^2P_{1/2,3/2}-1s^2S_{1/2}$	6.8	610 ±43
	12.12	Fe XVII	$2s^22p^5(^2P)4d^3D_1-2s^22p^6\ ^1S_0$	6.8	
	12.16	Fe XXIII	$1s^22s3s^1S_0-1s^22s2p^1P_1$	7.2	
12.82	12.82	Fe XX	$1s^22s^22p^{1/2}2p^{3/2}3d^{3/2}-2s^22p^3\ ^4S_{3/2}$	7.0	203 ± 30
	12.82	Fe XXI	$1s^22s2p^{1/2}2p^{3/2}3d^{5/2}-1s^22s2p^3\ ^3D_1$	7.0	
	12.85	Fe XX	$1s^22s^22p^{1/2}2p^{3/2}3d^{3/2}-2s^22p^3\ ^4S_{3/2}$	7.0	
	12.86	Fe XX	$1s^22s^22p^{1/2}2p^{3/2}3d^{5/2}-2s^22p^3\ ^4S_{3/2}$	7.0	
13.45	13.45	Ne IX	$1s2p^1P_1-1s^2\ ^1S_0$	6.6	586 ± 43
	13.46	Fe XIX	$2s^22p^3(^2D)3d^3S_1-2s^22p^4\ ^3P_2$	6.9	
13.70	13.70	Ne IX	$1s2s^3S_1-1s^2\ ^1S_0$	6.6	365 ± 33
14.20	14.21	Fe XVIII	$1s^22s^22p^{1/2}2p^3_{3/2}3d^{5/2}-2s^22p^5\ ^2P_{3/2}$	6.9	364 ± 25
	14.21	Fe XVIII	$2s^22p^4(^1D)3d^2D_{5/2}-2s^22p^5\ ^2P_{3/2}$	6.9	
15.01	15.01	Fe XVII	$2s^22p^5(^2P)3d^1P_1-2s^22p^6\ ^1S_0$	6.7	577 ± 31
15.20	15.20	Fe XIX	$1s^22s2p^2_{1/2}3s-2s2p^5\ ^3P_2$	6.9	262 ± 26
	15.18	O VIII	$4p^2P_{1/2,3/2}-1s^2S_{1/2}$	6.5	
16.00	16.00	O VIII	$3p^2P_{1/2,3/2}-1s^2S_{1/2}$	6.5	418 ± 26
	16.00	Fe XVIII	$2s^22p^4(^3P)3s^2P_{3/2}-2s^22p^5\ ^2P_{3/2}$	6.8	
16.80	16.77	Fe XVII	$2s^22p^5(^2P)3s^1P_1-2s^22p^6\ ^1S_0$	6.7	241 ± 25
17.06	17.05	Fe XVII	$2s^22p^5(^2P)3s^3P_1-2s^22p^6\ ^1S_0$	6.7	703 ± 38
17.64	17.62	Fe XVIII	$2s^22p^43P^2P_{3/2}-2s2p^6\ ^2S_{1/2}$	6.8	48 ± 17
18.62	18.63	O VII	$1s3p^1P_1-1s^2\ ^1S_0$	6.3	26 ± 17
18.96	18.97	O VIII	$2p^2P_{1/2,3/2}-1s^2S_{1/2}$	6.5	1218 ± 41
21.60	21.60	O VII	$1s2p^1P_1-1s^2\ ^1S_0$	6.3	224 ± 37
21.80	21.80	O VII	$1s2p^3P_1-1s^2\ ^1S_0$	6.3	50 ± 28
22.10	22.10	O VII	$1s2s^3S_1-1s^2\ ^1S_0$	6.3	135 ± 33
24.80	24.78	N VII	$^2P_{1/2,3/2}-1s^2S_{1/2}$	6.3	52 ± 20
33.57	33.73	C VI	$2p^2P_{1/2,3/2}-1s^2S_{1/2}$	6.2	169 ± 35

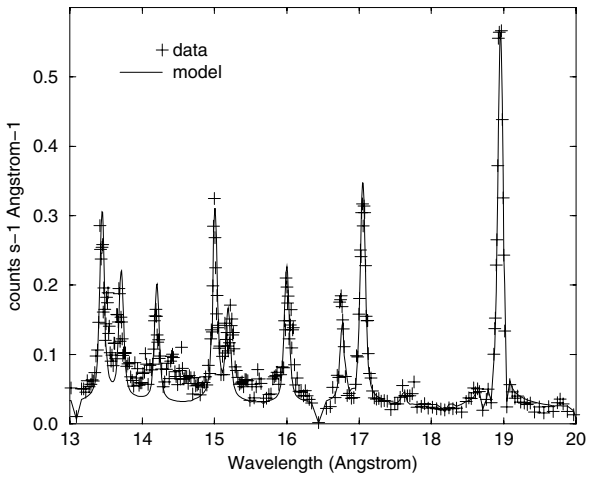

Fig. 5. Comparison of RGS 2 data with a best fit model folded with RGS2 response matrix. The model consists a three temperature Bremstrahlung continuum and Gaussian lines.

regions (Parkinson 1975) and in flares (McKenzie et al. 1982; Brown et al. 1986). These authors found that most of the solar measurements yield R value between 3 and 4. A few values significantly lower around $R \approx 2$ are related to flares or active regions. The *XMM–Newton* measurements of 44 Boo (R = 1.3–7.6) are comparable with the solar data, thus supporting the view that the physical properties of the O VII emiting layers in 44 Boo are not that different from those in the Sun.

5.3. Abundances and emission measure distribution

Following the approach proposed by Widing & Feldman (1989), a single differential emission measure DEM_L was defined for each individual RGS spectral line that is unblended and has a high ratio signal to noise (see Table 5). The element abundances $A(X)$ were initially set to the solar photospheric values produced by Grevesse et al. (1998). The Ne and O abundances relative to Fe were then adjusted in order to make the $(A(X) \times DEM_L)$ points lie along a common smooth curve. The method provide estimates of the ratios between element abundances and iron coronal abundance, relative to the solar photospheric ratio. The contribution functions $C(T)$ of the selected lines were calculated from the atomic physics parameters provided in the CHIANTI version 4.0 database (Landi et al. 1999; Dere et al. 2001) assuming collisional ionisation equilibrium.

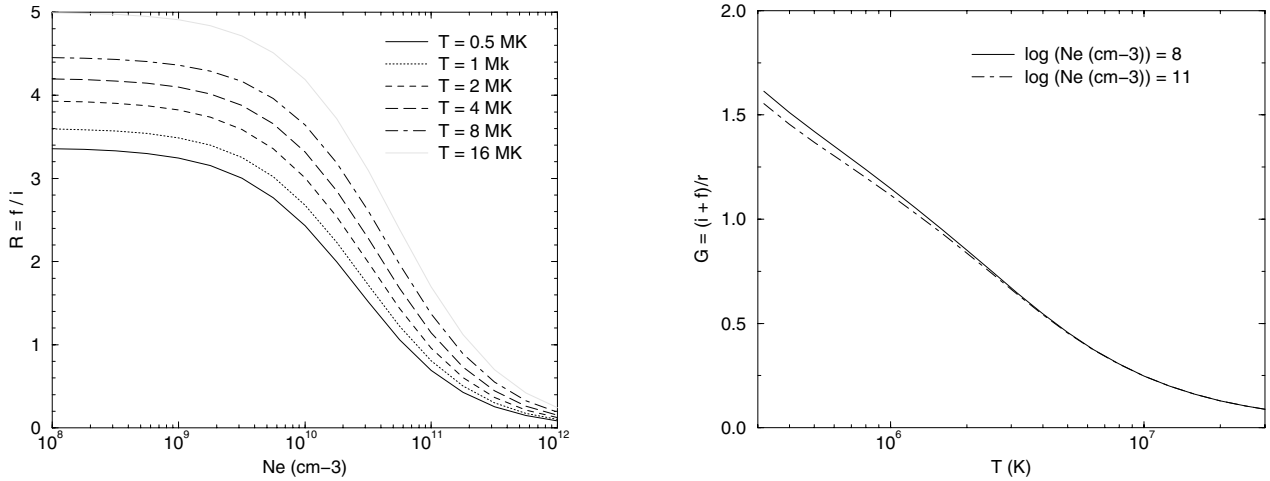

Fig. 6. *Left*: intensity ratio $R = f/i$ of the O VII forbiden ($\lambda = 22.12$ Å) and intercombination ($\lambda = 21.80$ Å) lines as a function of electron density. *Right*: ratio $G = (i + f)/r$ of the summed intensities of the OVII intercombination and forbiden lines over the intensity of the recombination line ($\lambda = 21.60$ Å) calculated using the CHIANTI database (Dere et al. 2001).

An electron density $n_e = 1.4 \times 10^{10}$ cm^{-3} was used based on the analysis result of the helium-like O VII triplet (see Sect. 5.2). The element abundance ratios derived from this analysis suggest abundances of oxygen and neon relative to iron of respectively 2.9 ± 0.4 and 2.1 ± 0.3. A comparison of the results with the solar case is difficult, since a large variety of solar coronal abundances have been reported, with variation from the photospheric values up to an order of magnitude (Feldman 1992; Raymond et al. 2001). These differences appear to be related to the first ionisation potential (FIP) of the various elements. The abundance of elements with low FIP (<10 eV, e.g. Fe) appear enhanced compared to those of the high FIP (>10 eV, e.g. Ne). In the past years, several works have investigated the presence of a FIP effect in stellar coronae (Drake et al. 1997; Laming & Drake 1999; Bowyer et al. 2000). From the study of a sample of RSCVn-like binary systems, Audard et al. (2003) suggested that the FIP bias is correlated with the activity level, changing from a marked inverse FIP effect in highly active stars to a possible solar-like effect in low activity stars. In agreement with this hypothesis, the above analysis suggests an inverse FIP effect in 44 Boo.

The total emission measure over the interval $\Delta \log T = 0.3$ centred around the temperature of maximum line formation was approximated as:

$$EM_{\rm L} = \frac{0.3 \times 4\pi d^2 \times F_{\rm obs}}{A(X) \times \int_T C(T)\, {\rm d}\log T} \quad (1)$$

where $F_{\rm obs}$ is the measured line flux and d the distance of 44 Boo ($d = 12.82$ pc). The line-based emission measure analysis is adequate, given the resolution of the data. However, Eq. (1) lead to a smoother emission measure than line-based, iterative techniques which integrate over the emissivity. This should be reminded when comparing the present analysis results to other studies which find strong bumps in the emission measure distribution. The emission measures derived from Fe, Ne and O line fluxes in RGS spectrum (see Table 5) are compared in Fig. 7 with the emission measure derived from the best fit MEKAL models to the EPIC spectra during the quiescent and flare periods (see Table 3). A good agreement is obtained between the emission measure determination using EPIC and RGS data with the exception of the $EM_{\rm L}$ value derived from the Fe XX lines at 12.82 Å. The analysis corroborates the conclusion that the emission measure of hot plasmas is evenly distributed over temperature within the range 2×10^6 K–2×10^7 K with the possible exception of a peak around 10^7 K reminiscent of a narrow bump around $\log T \approx 6.9$ observed in RSCVn's binaries and single active stars (Sanz-Forcada et al. 2002). Analysis of *Chandra* observations of 44 Boo performed on April 2000 also revealed an emission measure distribution characterized by a narrow peak at 0.8×10^7 K (Brickhouse et al. 2001). This aspect is debated but it has been suggested that a continuous flaring activity could produce such a hot component (Güdel 1997; Drake et al. 2000). Recent observations of Proxima Centauri (Güdel et al. 2004) and of the RS CVn system II Pegasi (Huenemoerder et al. 2001) confirm this hypothesis.

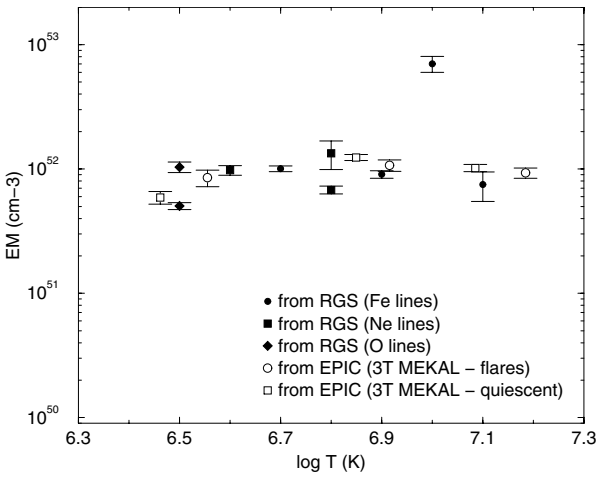

Fig. 7. Comparison between the emission measure distributions derived from EPIC flares and quiescent periods (see Table 3) and from Fe, Ne and O line fluxes in RGS spectrum (see Table 5).

6. Discussion

6.1. Structure of 44 Boo corona

44 Boo was observed in June 2001 by the *XMM–Newton* space observatory. The observation covers one orbital period of the close binary system. The X-ray light curve is in average constant with short 5 to 20% count rate increases reminiscent of flares. The spectral fitting of the EPIC spectra of 44 Boo at different periods with a three temperature components model suggests a corona configuration with little contribution from quiet regions. On the contrary the 0.2–0.7 keV temperature of the "cool" components is reminiscent of solar type active regions, while the hot ($T \approx 1.0$–1.3 keV) component may be caused by disruptions of magnetic fields associated with flaring activity. The best fit index of a power law model of the emission measure distributions of 44 Boo coronal plasmas (see Sect. 4) supports the hypothesis that solar-type loops are responsible for the X-ray emission. RGS observations of the O VII triplet (see Sect. 5.2) also suggest that the physical properties of the O VII emitting layers in 44 Boo are not that different from those in the Sun. The X-ray emission could originate from low-lying magnetic loops similar in size to those found in the solar corona, suggesting that 44 Boo corona has an appearence similar to the Sun's. The review of coronal activity by Vaiana & Rosner (1978) pointed out that the Sun, if completely covered by active regions, would have an X-ray luminosity of 20×10^{28} erg s^{-1}. When scaled to the surfaces of 44 Boo components ($R_1 \approx 0.87\ R_\odot$ and $R_2 \approx 0.66\ R_\odot$; Hill et al. 1989), X-ray luminosities of 15×10^{28} erg s^{-1} and 9×10^{28} erg s^{-1} are obtained for the primary and secondary companions, respectively. These values are lower than the observed luminosity of 44 Boo ($(23\text{–}27) \times 10^{28}$ erg s^{-1}) derived using *Hipparcos* parallaxes (see Table 2). They are comparable with the X-ray luminosity contribution ($\approx(12\text{–}18) \times 10^{28}$ erg s^{-1}) of the "cool" ($T <$ 0.8 keV) plasma components. Following a simple calculation, a corona around the two companions largely (50%–70%) filled with active regions is needed to explain the X-ray luminosity of the "cool" ($T < 0.8$ keV) plasmas with bright loops similar to those found in solar active regions. Assuming that these loop systems are static and each consists of similar loops of constant pressure p (dyn cm^{-2}), temperature T (K) and cross section, a characteristic loop length scale is obtained (Mewe et al. 1982) using the relation $T = 1400(pL)^{1/3}$ (Rosner et al. 1978):

$$L_{10} = 7.4 \times F \times T_7^4 \times EM_{52}^{-1} \times (R/R_\odot)^2 \quad (2)$$

where L_{10} is the loop half length in units of 10^{10} cm, T_7 is the coronal temperature in unit of 10^7 K, and EM_{52} is the emission measure in units of 10^{52} cm^{-3}. Inserting the observed temperature and emission measures (see Table 3) of the cold ($T <$ 0.8 keV) components, characteristic loop sizes in the range $(0.7\text{–}1.1) \times 10^9$ cm and $(11\text{–}23) \times 10^9$ cm are obtained for temperatures of the two coolest plasma components in the ranges $T_1 = (2.9\text{–}3.6) \times 10^6$ K and $T_2 = (7.1\text{–}8.2) \times 10^6$ K, respectively. A value $L \approx 4 \times 10^8$ cm of the typical loop length associated with the cool plasma component was deduced from the pressure and density derived from the O VII helium like triplet (see Sect. 5.2). This supports the existence of low-lying loops on 44 Boo similar to the loops found in the solar corona. On the other end, the possible presence of loops systems with characteristic lengths greater than 11×10^9 cm corresponding to a significant fraction of the stars radii is somewhat puzzling. On the Sun, loop structures are occasionally found at large heights, but they have low densities and never contribute significantly to the overall X-ray emission. Also, the RTV scaling law neglects gravity, assumes a constant cross-section, uniform heating, constant pressure and a monotonic increase of temperature with height. Since it turns out that $(11\text{–}23) \times 10^9$ cm loop lengths derived using the RTV model are comparable with the pressure scale height H on the star ($H \approx 3 \times 10^{10}$ cm), the assumption of constant pressure in these large loops is barely justified. Furthermore, Schrijver et al. (1989) questioned the assumption of constant loop cross section. Schrijver (1987) noticed that coronal condensation over solar bipolar regions has a projected area roughly an order of magnitude larger than the area of the underlying photospheric plage, suggesting the ratio Γ of the loop cross section at the apex to the cross section at the footpoint is approximately $\Gamma \approx 10$. Vesecky et al. (1979) made numerical calculations for loop with cross sections increasing with height in a way resembling a line dipole. They find that the scaling law is modified by the change in the loop cross section with height. Schrijver et al. (1989) note that their numerical results can be conveniently approximated by $T = 1400\ \Gamma^{-0.1} \times (pL)^{1/3}$. Using this modified law, one finds that the constant Γ enters Eq. (1) to the sixth power and could dramatically increase the loop half-length making it inconsistent with the constant pressure hypothesis. This suggests the presence of large loops on 44 Boo that support the existence of an extended corona encompassing a low-lying loop system similar to that found in the solar corona. This picture could explain the absence of eclipses in the X-ray light curves.

6.2. Flaring activity on 44 Boo

The X-ray light curve of 44 Boo is relatively constant in average with 5 to 20% count rate increases of about a ksec duration around phase 1.3, 1.65 and 1.9. The temperature of the hottest plasma component is higher during these high count rate periods. These rapid count rate variations and high plasma temperatures are reminiscent of flares also observed during previous *Chandra* observations (Brickhouse et al. 2001). However, compared with other active binary systems such as RSCVn or BY Dra (Dempsey et al. 1993), 44 Boo has relatively less material at temperatures higher than 10^7 K and the temperature of this hot plasma component appear to be lower. Different approaches have been proposed to estimate characteristic parameters and in particular the size of flaring regions. Analytic approaches (van den Oord & Mewe 1989; Pallavicini et al. 1990; Hawley et al. 1995) using only rise and decay time are adequate for the analysis of a large flare for which only light curves are available. However, they tend to overestimate the size of the flaring regions, in particular in the presence of significant heating during the decay (Favata & Schmitt 1999). As an extreme example, assuming that the three events around phase 1.3, 1.65 and 1.9 during *XMM–Newton* revolution 274 are each related

to a single flare event, we estimated a lower limit of the density during these flares by equating the measured decay time, the so-called e-folding time, to the radiative cooling time (Pallavicini et al. 1990), i.e. $\tau_{\rm rad} = 3kT/nP(T)$ where n is the density, T the coronal temperature, k the Boltzmann constant and $P(T)$ the radiative loss function for unit emission measure. Using $P(T) \approx 2 \times 10^{-23}$ erg cm^3 s^{-1} for temperatures in the range (1–4) $\times$ 10^7 K (Mewe et al. 1985), we found $n > 2 \times 10^{11}$ cm^{-3} for a characteristic decay time of 1.5 ks. For stellar flares decay times, typically in a range 10^3–10^5 s, Reale (2002) estimated loop lengths in the range 10^{10}–10^{11} cm for a maximum temperature $T_{\rm max} = 1.9 \times 10^7$ K. In general, Serio et al. (1991) showed that a flaring loop starting from equilibrium decays freely with a global thermodynamic time scale linearly dependent on the loop length $\tau_{\rm th} = 12 \times L_{10} \times T_7^{-1/2}$. Hence, the fast decays on 44 Boo would imply loop lengths of about 16×10^9 cm, i.e. comparable in size to the two-ribbon flares observed on the Sun and may be associated to magnetic reconnection phenomena in the large loops system previously inferred. However, this simplistic analysis is based on some crucial assumptions which may not hold. In particular, the loop length would be significantly overestimated in case the decay does not start from equilibrium condition or in case heating is not totally absent during the decay phase.

7. Summary

44 Boo B, a W UMa-type binary system, was observed in June 2001 during its entire revolution period with the *XMM–Newton* observatory. The count rate in the 0.3 to 2 keV band is constant in average with intermittent 5 to 20% count rate increases reminiscent of flares. The spectral fitting of the EPIC spectra of 44 Boo suggests that the active corona around the two companions is densely filled with bright loops similar to those found in solar-type active regions. The hottest part ($kT \approx 1.0$–1.3 keV) of the emission measure distribution may be caused by disruptions of magnetic fields associated with flaring activity. A typical loop length $L \approx 4 \times 10^8$ cm associated with the cool plasma component was deduced from the pressure $P_{\rm e} \approx 8$ dyn cm^{-2} and density $n_{\rm e} \approx 14 \times 10^9$ cm^{-3} estimated from the RGS observation of the O VII helium like triplet. This supports the existence of low-lying loops on 44 Boo similar to the loops found in the solar corona. We argue that this low-lying loop system may be overlaid by larger loops. Magnetic reconnection phenomena in this large loops system may explain the characteristic flare decay time in the light curve that implies loop lengths of about 15×10^9 cm, i.e. comparable in size to the two-ribbon flares observed on the Sun. An extended corona on 44 Boo would explain the absence of eclipses in its X-ray light curve. The average element abundance in 44 Boo corona is found to be lower than the solar photospheric value. The analysis of RGS spectra indicates enhanced abundances of oxygen and neon relative to iron which suggest an inverse FIP effect. Compared with other active binary systems such as RSCVn or BY Dra, 44 Boo has relatively less material at temperatures higher than 10^7 K and the temperature of it hottest plasma appears to be lower.

Acknowledgements. I thank my colleagues from the *XMM–Newton* Science Operation Center for their support in implementing the observations. CHIANTI is a collaborative project involving NRL (USA), RAL (UK) and the Universities of Florence (Italy) and Cambridge (UK). I am grateful to the anonymous referee for the helpful comments that allowed to improve the paper.

References

Anders, E., & Grevesse, N. 1989, Geochim. Cosmochim. Acta, 53, 197
Antiochos, S. K., & Noci, G. 1986, ApJ, 301, 440
Arnaud, K., & Dorman, B. 2001, XSPEC User's Guide for version 11.1, http://heasarc.gsfc.nasa.gov/docs/xanadu/xspec/manual/
Audard, M., Güdel, M., & Mewe, R. 2001a, A&A, 365, L318
Audard, M., Behar, E., Güdel, M., et al. 2001b, A&A, 365, L329
Audard, M., Güdel, M., Sres, A., et al. 2003, A&A, 398, 1137
Bowyer, S., Drake, J. J., & Vennes, S. 2000, ARA&A, 38, 231
Brickhouse, N. S., & Dupree, A. K. 1998, ApJ, 502, 918
Brickhouse, N. S., Dupree, A. K., & Young, P. R. 2001, ApJ, 562, L75
Brown, W. A., Bruner, M. E., Acton, L. W., et al. 1986, ApJ, 301, 981
Cruddace, R. G., & Dupree, A. K. 1984, ApJ, 277, 263
Dempsey, R. C., Linsky, J. L., Schmitt, J. H. M. M., et al. 1993, ApJ, 413, 333
den Herder, J. W., Brinkman, A. C., Kahn, S. M., et al. 2001, A&A, 365, L7
Dere, K. P., Landi, E., Young, P. R., & Del Zanna, G. 2001, ApJS, 134, 331
Dickey, J. M., & Lockman, F. J. 1990, ARA&A, 28, 215
Drake, J. J., Laming, J. M., & Widing, K. G. 1997, ApJ, 478, 403
Drake, J. J., Peres, G., Orlando, S., et al. 2000, ApJ, 545, 1074
Dupree, A. K., Brickhouse, N. S., Doschek, G. A., et al. 1993, ApJ, 418, L41
Ehle, M., Breitfellner, M., Dahlem, M., et al. 2001, The XMM–Newton Users' Handbook, http://xmm.vilspa.esa.es/user/A02/uhb/xmm_uhb.html
ESA 1997, The Hipparcos Catalogue, ESA SP-1200
Favata, F., & Schmitt, J. H. M. M. 1999, A&A, 350, 900
Feldman, U. 1992, Phys. Scr., 46, 202
Freeman, F. F., & Jones, B. B. 1970, Sol. Phys., 15, 228
Gabriel, A. H., & Jordan, C. 1969, MNRAS, 145, 241
Golub, L., & Pasachoff, J. M. 1997, in The Solar Corona (Cambridge UK: Cambridge University Press)
Gondoin, P. 2004, A&A, 415, 1113
Gondoin, P., Aschenbach, B., Erd, C., et al. 2000, SPIE Proc., 4140, 1
Grevesse, N., & Sauval, A. J. 1998, Space Sci. Rev., 85, 161
Griffiths, N. W., & Jordan, C. 1998, ApJ, 497, 1998
Güdel, M. 1997, ApJ, 480, L121
Güdel, M., Audard, M., Briggs, K., et al. 2001, A&A, 365, L336
Güdel, M., Audard, M., Reale, F., et al. 2004, A&A, 416, 713
Hawley, S. L., Fisher, G. H., Simon, T., et al. 1995, ApJ, 453, 464
Hill, G., Fisher, W. A., & Holmgren, D. 1989, A&A, 211, 81
Huenemoerder, D. P., Canizares, C. R., & Schulz, N. S. 2001, ApJ, 559, 1135
Jansen, F., Lumb, D., Altieri, B., et al. 2001, A&A, 365, L1
Landi, E., Landini, M., Dere, K. P., et al. 1999, A&AS, 135, 339
Laming, J. M., & Drake, J. J. 1999, ApJ, 516, 324
Lu, W., Rucinski, M. R., & Ogloza, W. 2001, ApJ, 122, 402
McGale, P. A., Pye, J. P., & Hodgkin, S. T. 1996, MNRAS, 280, 627
McKenzie, D. L., Rugge, H. R., Underwood, J. H., et al. 1978, ApJ, 221, 342
McKenzie, D. L., & Landecker, P. B. 1982, ApJ, 259, 372

Mewe, R., Gronenschild, E. H. B. M., Heise, J., et al. 1982, ApJ, 260, 233
Mewe, R., Gronenschild, E. H. B., & van den Oord, G. H. J. 1985, A&A, 62, 197
Mewe, R., Raassen, A. J. J., Drake, J. J., et al. 2001, A&A, 368, 888
Ness, J. U., Mewe, R., Schmitt, J. H. M. M., et al. 2001, A&A, 367, 282
Pallavicini, R., Tagliaferri, G., & Stella, L. 1990, A&A, 228, 403
Parkinson, J. H. 1975, Sol. Phys., 42, 183
Pradhan, A. K. 1982, ApJ, 263, 477
Raymond, J. C., Mazur, J. E., Allegrini, F., et al. 2001, in Solar and Galactic Composition, AIP Conf. Proc., 598, 49
Reale, F., Peres, G., & Orlando, S. 2001, ApJ, 557, 906
Reale, F. 2002, in Stellar Coronae in the Chandra and XMM Era, ed. F. Favata, & J. Drake, ASP Conf. Ser., 277, 103
Rosner, R., Tucker, W. H., & Vaiana, G. S. 1978, ApJ, 220, 643
Rucinski, S. M. 1985, MNRAS, 215, 615
Rucinski, S. M. 1998, AJ, 115, 303
Sanz-Forcada, J., Brickhouse, N. S., & Dupree, A. K. 2002, ApJ, 570, 799
SAS 2001, XMM-Newton Science Analysis System, Reference Documentation, `http://xmm.vilspa.esa.es/user/sas_top.html`
Schilt, J. 1926, ApJ, 64, 215
Schmitt, J. H. M. M., Collura, A., Sciortino, S., et al. 1990, ApJ, 365, 704
Schrijver, C. J. 1987, A&A, 180, 241
Schrijver, C. J., Lemen, J. R., & Mewe, R. 1989, ApJ, 341, 484
Serio, S., Reale, F., Jakimiec, J., et al. 1991, A&A, 241, 197
Stepien, K., Schmitt, J. H. M. M., & Voges, W. 2001, A&A, 370, 157
Strüder, L., Briel, U., Dennerl, K., et al. 2001, A&A, 365, L18
Turner, M. J. L. T., Abbey, A., Arnaud, M., et al. 2001, A&A, 365, L27
Vaiana, G. S., & Rosner, R. 1978, ARA&A, 16, 393
van den Oordt, G. H. J., & Mewe, R. 1989, A&A, 213, 245
Vesecky, J. F., Antiochos, S. K., & Underwood, J. H. 1979, ApJ, 233, 987
Vilhu, O., & Heise, J. 1986, ApJ, 311, 937
Vilhu, O., Neff, J. E., & Rahunen, T. 1989, A&A, 208, 201
Widing, K. G., & Feldman, U. 1989, ApJ, 344, 1046